# Two sides of a fault: Grain-scale analysis of pore pressure control on fault slip

Zhibing Yang and Ruben Juanes

Phys. Rev. E **97**, 022906 — Published 21 February 2018

DOI: 10.1103/PhysRevE.97.022906

# The two sides of a fault: grain-scale analysis of pore pressure control on fault slip

Zhibing Yang[1, 2, 3] and Ruben Juanes[1, 4, *]

[1] *Department of Civil and Environmental Engineering, Massachusetts Institute of Technology, Cambridge, Massachusetts, USA.*
[2] *Department of Earth Sciences, Uppsala University, Uppsala, Sweden.*
[3] *State Key Laboratory of Water Resources and Hydropower Engineering Science, Wuhan University, Wuhan 430072, China.*
[4] *Department of Earth, Atmospheric and Planetary Sciences, Massachusetts Institute of Technology, Cambridge, Massachusetts, USA.*

(Dated: February 12, 2018)

Pore fluid pressure in a fault zone can be altered by natural processes (e.g., mineral dehydration and thermal pressurization) and industrial operations involving subsurface fluid injection/extraction for the development of energy and water resources. However, the effect of pore pressure change on the stability and slip motion of a preexisting geologic fault remains poorly understood; yet it is critical for the assessment of seismic hazard. Here, we develop a micromechanical model to investigate the effect of pore pressure on fault slip behavior. The model couples fluid flow on the network of pores with mechanical deformation of the skeleton of solid grains. Pore fluid exerts pressure force onto the grains, the motion of which is solved using the discrete element method. We conceptualize the fault zone as a gouge layer sandwiched between two blocks. We study fault stability in the presence of a pressure discontinuity across the gouge layer, and compare it with the case of continuous (homogeneous) pore pressure. We focus on the onset of shear failure in the gouge layer, and reproduce conditions where the failure plane is parallel to the fault. We show that when the pressure is discontinuous across the fault, the onset of slip occurs on the side with the higher pore pressure, and that this onset is controlled by the maximum pressure on both sides of the fault. The results shed new light on the use of the effective stress principle and the Coulomb failure criterion in evaluating the stability of a complex fault zone.

**PACS numbers:**

## I. INTRODUCTION

Geological faults form as a result of the failure of rock in the Earth's crust, and slip along an existing fault can generate hazardous earthquakes. It has long been known that man-made fluid pressure changes due to factors such as impoundment of reservoirs, surface and underground mining, withdrawal of fluids and gas from the subsurface, and injection of fluids into underground formations, are capable of reactivating pre-existing faults and thus inducing earthquakes [1–5]. One of the well-known early examples is the 1960s Denver Earthquake series, which was induced by a deep waste fluid disposal well at the Rocky Mountain Arsenal [1]. Not only can pore pressure be affected by anthropogenic processes, it can also be altered in natural geologic systems. For example, earthquake rupturing along a highly localized shear zone can generate enough heat to cause local temperature rise and the accompanying pore pressure increase due to expansion of pore fluid. This so-called thermal expansion process has been proposed as one of the key mechanisms to explain dynamic fault weakening [6–8]. Despite the important control pore pressure has on slip and faulting behavior, the detailed dynamics and mechanisms involved in fault reactivation remain poorly constrained [9, 10].

Fault zones can have very complex internal structures, including the continuity of the fault rocks, the distribution and segmentation of slip surfaces, and the orientation, distribution and connectivity of subsidiary faults and fractures [11]. Flow and transport properties of fault zones can vary significantly from site to site, depending on the internal structure. A fault zone typically consists of two sub-structures: the fault core and the damage zone. The primary characteristic of fault cores is grain size reduction due to mechanical pulverization. The hydraulic properties of the fault core (gouge materials) can be very different from the fault damage zones and the undamaged host rock. Fault gouge is usually composed of fine particles/fragments. In many cases, the permeability of fault cores can be several orders of magnitude lower than that of a reservoir rock [12] and often acts as an impermeable boundary for fluid flow. In addition, hydraulic connectivity across the fault may be lost, for example, due to clay smearing or juxtaposition of a relatively high permeability reservoir rock with a low permeability rock from another formation [13]. Juxtaposition of two different rock types can also lead to difference in frictional strength on the two sides of a fault.

Numerical modeling of coupled flow and geomechanics is a valuable tool in assessing seismic hazard in large-scale reservoir systems. The effective stress principle together with the Mohr–Coulomb failure criterion has been applied in numerical modeling to explain fault reactivation due to fluid injection and to predict fault stability [see e.g., 14–19]. Reactivation of faults may occur if the shear stress on the fault exceeds the fault strength which is governed by the frictional properties and the effective normal

* Correspondence to: juanes@mit.edu

stress. It is unclear, however, how conventional Mohr–Coulomb theory should be applied to the case where there is a substantial pressure difference across the fault zone due to fault cores that are considered impermeable over the time scale of interest. In their coupled multiphase flow and geomechanics model, Jha and Juanes [17] proposed to calculate the fault pressure in the failure criterion to be the maximum of pressures on both sides of the fault, which is represented by a 2D interface element in a 3D mesh. If the fault pressure is taken as the arithmetic average across the fault or is obtained from volume element based pressure, a coupled modeling analysis may predict a higher fault strength at any given time and result in a delayed onset of fault reactivation (than that with the maximum pressure), which, consequently, can lead to erroneous estimations of maximum fluid injection rate/volume in practical situations. Therefore, it is critical to carefully examine the role of pressure discontinuity in controlling fault stability.

Theoretical studies based on the continuum approach [see e.g., 20, 21] have addressed the issue of pore pressure discontinuity due to existence of material with different hydraulic parameters across the fault. Considering a spontaneously propagating rupture along an interface between dissimilar poroelastic materials, these studies have provided important insights on how pore pressure change induced by an imposed fast slip between dissimilar poroelastic materials can influence the stability of earthquake ruptures. In addressing the important issue of fault dynamic weakening by flash heating and thermal pressurization, Rice [7] ruled out the possibility that shear deformation in the gouge is distributed across the gouge during dynamic earthquake slip.

Fault gouge can be considered a dense granular material whose deformation is controlled by the collective motion of the constituent particles. Continuum models of deforming granular material rely on constitutive laws in which the formulation of continuum deformation requires a projection scheme to relate the continuum deformation to the underlying motion of the grains [22]. In contrast, models based on the discrete element method (DEM) treat individual particles explicitly, and have effectively captured emergent phenomena, such as shearing banding and stick-slip in deforming granular materials [see e.g., 22–30]. In this study, we adopt a DEM framework, and instead of imposing slip, we simulate emergence of slip around a fault gouge layer with two interfaces with the bounding material. Numerical simulations—mostly based on DEM [e.g., 25–27, 29, 31, 32]—have been used to understand the fundamental role gouge material plays in determining fault frictional properties and strength. These previous numerical studies on faulting or shearing, however, have not considered the effect of pore fluid pressure coupling. We present evidence, based on a grain-scale analysis, in support of the choice of using the maximum fluid pressure across the fault for evaluation of the failure criterion.

In short, accurate prediction of fault stability requires detailed understanding of the role of pore pressure. In this work, we develop a micromechanical model at the grain scale and perform one-way coupled simulations to investigate the effect of pore pressure on fault slip behavior. We consider a block–gouge system where the block represents the fault walls. We study fault stability in the presence of a pressure discontinuity across the gouge layer, and compare it with cases of homogeneous pore pressures. We focus on the onset of shear failure along the block–gouge interfaces, and provide new insights on the use of the effective stress principle and the Coulomb failure criterion in evaluating the stability of a complex fault zone.

## II. METHODS

We develop a three-dimensional micromechanical model, which is based on the discrete element method (DEM) coupled with a pore network flow (PNF) model, illustrated in Fig. 1. In the DEM, the solid phase is represented by spherical grains and contact interaction among them. The spatial arrangement of grains forms an interconnected void space, from which a pore network, comprised of pore bodies and pore throats, is extracted through tetrahedral (weighted Delaunay) tessellation of grain centroids (see Fig. 1(a)–(b)). The pore body volumes and the pore throat conductances are calculated based on the void space geometry. The fluid in the pore network interacts with the solid grains, giving rise to hydro-geomechanical coupling. On the one hand, the pore fluid exerts pressure forces onto the grains, resulting in modified force balance and motion of the grains as compared to that in the dry system. On the other hand, deformation of the solid phase through rearrangement of the grains can also change the pore pressure and the pore-network topology. Our model updates the tetrahedral tessellation, and hence the pore-network (including its pore volumes and pore throat conductances), regularly during a simulation. The frequency of this updating procedure can be preset according to the timestep size or a certain threshold displacement of the grains. The PNF model solves the pressure evolution based on Darcian flow in the pore network and calculates the pressure forces onto the solid particles. Compared with other DEM-based poromechanical coupling approaches, including microscale models where fluid pressure is resolved below the pore scale [e.g., 33–35] and continuum-scale models in which flow is solved on a coarse grid at the scale of multiple grains [e.g., 36], the PNF approach [37–39] is advantageous in that it avoids the high computational cost in the microscale models and the inability to accurately describe the fluid–solid interaction at the particle scale in the continuum-scale models. Below, we describe the numerical model in detail.

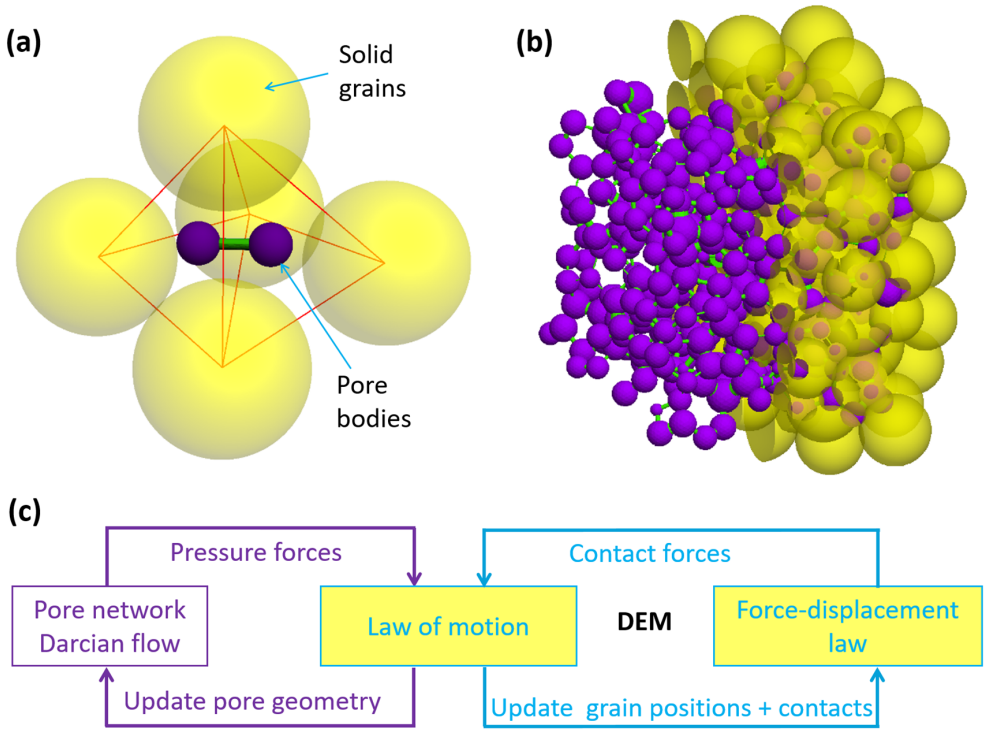


FIG. 1. Schematic of the coupled hydromechanical model based on the Discrete Element Method (DEM) and a Pore Network Flow (PNF) model. (a) pore network in a five-grain setup (transparent yellow spheres); the pores are shown by purple spheres and the throat by a green cylinder; the edges of the tetrahedral tessellation are shown with red lines. Each pore is composed of the void space within a tetrahedron whose four nodes are the centers of the surrounding grains. Each throat is defined by the open area within a triangular face of a tetrahedron. The pore volumes and throat conductances are calculated based on local geometry. (b) grain pack (cut in half and rendered in 50% opaque yellow color) and accompanying pore network. (c) schematic of the couplings in the DEM–PNF model.

### A. Discrete element method

Our three-dimensional (3D) micromechanical model couples the discrete element method (DEM) and a pore-network fluid flow model. The modeling concept is based on the idea of two interacting, overlapping networks: one for the solid matrix and the other for the pore fluid [37, 38]. In DEM, spherical grains are numerically generated and the mechanics of the grain motions are solved. The translational motion of each grain in the system is governed by Newton's second law:

$$m_i \ddot{\mathbf{x}}_i = \sum_j \mathbf{F}_j^{\mathrm{c}} + \sum_k \mathbf{F}_k^{\mathrm{p}}, \tag{1}$$

where $m_i$ is the mass of $i$th grain whose position vector is $\mathbf{x}_i$, $\mathbf{F}_j^{\mathrm{c}}$ is the force applied on contact $j$ of the grain, and $\mathbf{F}_k^{\mathrm{p}}$ is the pressure force applied by $k$th pore surrounding the grain. The pressure force on $i$th grain by $k$th pore is calculated by:

$$\mathbf{F}_k^{\mathrm{p}} = \int_{\partial\Gamma_k^i} p_k \mathbf{n}\, \mathrm{d}s, \tag{2}$$

where $\partial\Gamma_k^i$ is the fluid–solid interface for $i$th grain and $k$th pore (with pore pressure $p_k$), $\mathbf{n}$ is the unit vector pointing from the centroid of the pore to the centroid of the grain. The rotational motion of each grain is described by:

$$\mathbf{I}_i \ddot{\boldsymbol{\theta}}_i = \sum_j \mathbf{M}_j^{\mathrm{c}}, \tag{3}$$

where $\mathbf{I}_i$ is the tensor of moments of inertia of grain $i$ with the vector of rotation angles $\boldsymbol{\theta}_i$ around its centroid, and $\mathbf{M}_j^{\mathrm{c}}$ is the moment acting on grain $i$ through contact $j$. The pressure force points from the centroid of a pore to the centroid of a grain; it does not induce moments on grains. We use the PFC3D code [40] to solve the equations of motion simultaneously for all grains in the system and to integrate these equation in time.

While fluid pressure influences grain motions through the application of pressure forces, the movement of grains deforms the individual pores, thus altering the pore pressure distribution. At the same time, the pore pressure evolution is subject to Darcian flow under the prevailing hydrodynamic conditions. To solve the fluid pressure with the above interactions taken into account, we develop a 3D numerical model for pore-network flow (il-

lustrated with Fig. 1 and Fig. 2), which is coupled to PFC3D. This model is described in detail below.

### B. Pore network flow model

As a discretization of the pore space, a pore network is extracted from each numerically generated granular pack (see Fig. 1). We perform a 3D weighted Delaunay triangulation in which each vertex is the centroid of a grain and each tetrahedron contains a pore (Fig. 2).

Using basic geometry, we calculate the volume of each pore $V_i$ by subtracting the volume of the solid part $V_i^{\mathrm{s}}$ from the volume of a tetrahedron $V_i^{\mathrm{tet}}$:

$$V_i = V_i^{\mathrm{tet}} - V_i^{\mathrm{s}}. \tag{4}$$

The volume of the solid part $V_i^{\mathrm{s}}$ is calculated as:

$$V_i^{\mathrm{s}} = \sum_{j=1}^{4} V_j^{\mathrm{sc}} - \sum_{k=1}^{6} V_k^{\mathrm{so}}, \tag{5}$$

where $V_j^{\mathrm{sc}}$ is the volume of the spherical cone of each grain $j$ ($j$ = 1,2,3,4) inside the tetrahedron, and $\sum_{k=1}^{6} V_k^{\mathrm{so}}$ is the total solid overlap volume of the six possible grain–grain contacts. Note that we do not consider the overlap volume shared by more than two spheres because this overlap scenario does not occur in our simulations owing to the fact that only very small overlap distances are induced by realistic external forces. The pore throat length $l_{ij}$ is taken as the distance between the centroids of tetrahedron $i$ and tetrahedron $j$. The pore throat conductance $C_{ij}$ is calculated based on the minimum cross-sectional area $A_{ij}^{\mathrm{pt}}$ on a triangular face between tetrahedron $i$ and $j$, the perimeter $P_{ij}^{\mathrm{pt}}$ associated with $A_{ij}^{\mathrm{pt}}$, and the fluid viscosity $\eta$ as [38, 41]:

$$C_{ij} = \frac{3{A_{ij}^{\mathrm{pt}}}^3}{5\eta {P_{ij}^{\mathrm{pt}}}^2}. \tag{6}$$

The pore volumes, throat conductances, and throat lengths are all functions of the grain positions and radii, and are thus subject to change when the solid phase deforms. In our model, we update these parameters on a regular basis at a selected time interval.

When local accumulated grain displacement becomes large, i.e., comparable to the grain radius, the initial triangulation may no longer faithfully represent the pore space constrained by the new grain positions. For example, this occurs when one grain slips past another. Using the initial triangulation for pressure solution and force calculations may bring a source of error. In order to minimize the potential error from the deteriorated representation of the pore space by the pore network due to large local deformation, we update the triangulation regularly during a simulation.

Fluid mass balance over an pore $V_i$ gives the following equation:

$$\frac{\delta V_i}{\delta t} + V_i^{\mathrm{w}} \beta_f \frac{\delta p_i}{\delta t} = -\sum_j q_{ij}, \tag{7}$$

where $\delta V_i$ and $\delta p_i$ are the pore volume change (due to matrix deformation) and the pore pressure change after a time step $\delta t$, respectively, $V_i^{\mathrm{w}}$ is the volume of fluid in pore $i$ ($V_i^{\mathrm{w}} = \delta V_i$ in the case of pore network), $\beta_w$ is the compressibility of the fluid and $q_{ij}$ is the flux out of the pore domain to pore $j$ through pore throat $(i, j)$. The flux $q_{ij}$ is calculated as:

$$q_{ij} = C_{ij} \frac{p_i - p_j}{l_{ij}}. \tag{8}$$

In Eq. (7), the two terms on the left hand side are analogous to the storage term in the diffusion equation of compressible flow in porous media. The pore pressure solution of Eq. (7) with Eq. (8) plugged in can be obtained by using two approaches. The first is an explicit scheme [38] with the fluxes calculated using pressure gradients from the last time step, giving the following equation to update fluid pressure in each pore:

$$\delta p_i = \frac{1}{\beta_w V_i} \left( -\delta V_i - \sum_j q_{ij} \delta t \right). \tag{9}$$

Note that numerical stability of the explicit pressure solution [Eq. (9)] imposes a timestep limit, and thus the timestep should be carefully chosen in a numerical simulation.

In this study, we propose the second approach, which employs an implicit finite-volume scheme:

$$\frac{\delta V_i}{\delta t} + V_i \beta_w \frac{p_i^{n+1} - p_i^n}{\delta t} = -\sum_j C_{ij} \frac{p_i^{n+1} - p_j^{n+1}}{l_{ij}}, \tag{10}$$

where the superscripts $n$ and $n+1$ represent the current timestep and the timestep to be advanced, respectively. The implicit scheme enjoys unconditional stability in terms of timestepping. Writing Eq. (10) for all pores results in a system of linear equations for pore pressure in matrix form:

$$\mathbf{\Lambda p^{n+1}} = \mathbf{b}, \tag{11}$$

with entries $\lambda_{i,j}$ in $\mathbf{\Lambda}$ and $b_i$ in $\mathbf{b}$ calculated, respectively, by:

$$\lambda_{i,j} = \begin{cases} \frac{V_i \beta_w}{\delta t} + \sum_{k=1}^{4} \frac{C_{ik}}{l_{ik}} & \text{if } i = j \\ -\frac{C_{ij}}{l_{ij}} & \text{if } i \neq j \end{cases} \tag{12}$$

and

$$b^i = -\frac{\delta V_i}{\delta t} + \frac{V_i \beta_w p_i^n}{\delta t}. \tag{13}$$

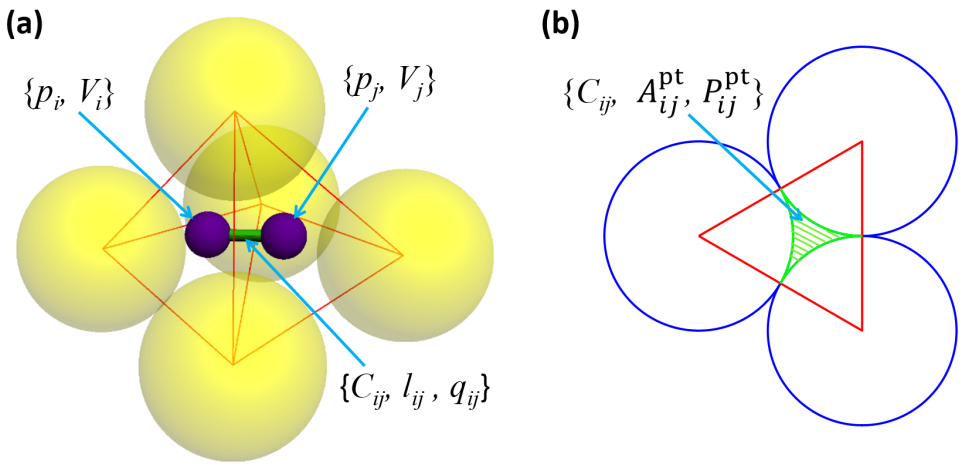


FIG. 2. Illustration of triangulation, pore network, and pore throat. (a) pore network in a five-grain setup; the pores are shown by purple spheres and the throat by a green cylinder; the edges of the tetrahedral tessellation are shown in red. Each pore is composed of the void space within a tetrahedron whose four nodes are the centers of the surrounding grains. The two pores have volumes $V_i$ and $V_j$, and pressures $p_i$ and $p_j$. Each pore throat having conductance $C_{ij}$ and length $l_{ij}$ is defined as the connection between two neighboring pores ($V_i$ and $V_j$) through the void space. (b) The pore throat conductance $C_{ij}$ is calculated based on the minimum cross-sectional area $A_{ij}^{\mathrm{pt}}$ on a triangular face between tetrahedron $i$ and $j$ (the shaded area), and the perimeter $P_{ij}^{\mathrm{pt}}$ associated with $A_{ij}^{\mathrm{pt}}$.

Pressure solutions obtained using the explicit and the implicit schemes take into account both the pressure diffusion and the effect of deformation of the solid matrix obtained from DEM. Thus, this fluid flow formulation coupled with the DEM framework captures the two-way hydro-mechanical coupling under single-phase flow.

### C. Contact behavior

Two rheological models for contact behavior are used in this study. The first is a linear elastic–frictional contact law described in more detail in Cundall and Strack [42]; this contact model is used for contacts on gouge particles. In this contact model, the contact force is produced by linear springs with constant normal and shear stiffnesses, $k_{\mathrm{c}}^{\mathrm{n}}$ and $k_{\mathrm{c}}^{\mathrm{s}}$. The linear springs cannot sustain tension—the contact law is deactivated when the surface gap $g_{\mathrm{s}} > 0$, and slip is accommodated by imposing a Coulomb limit on the tangential force using a constant friction coefficient $\mu$. The second, which is used for contacts between the block particles, is the linear contact bond model described in more detail in Potyondy and Cundall [43]. This contact rheology provides the behavior of a linear elastic and either bonded or frictional interface that carries a force. The interface does not resist relative rotation and is either bonded or unbonded. If bonded, the behavior is linear elastic until the strength limit is exceeded and the bond breaks, making the interface unbonded. If unbonded, the behavior is linear elastic-frictional—equivalent to the first contact model.

### D. Block–gouge system

Gouge materials play an important role in earthquake nucleation. They have been extensively studied experimentally [e.g., 10, 44–49], often with the primary interest of examining their frictional properties and slip instability characterized by the rate and state friction laws [50, 51]. A recent experimental study [49] reported that increasing pore-fluid pressure leads to a decrease in the internal friction coefficient of carbonate gouge sample, but the mechanisms behind this observation remain unexplained. Geller *et al.* [52] developed a 2D experimental setup of a plate-granular rods system under dry condition, and analyzed the stick-slip dynamics of the granular layer undergoing shear using digital image analysis. Despite recent advances in 3D experimental techniques in measuring forces at the grain scale [53, 54], real time imaging of grain displacement and forces remains challenging for granular packs in dynamic deformation.

Here, we apply the coupled DEM–PNF model described above to a representation of a fault zone consisting of a gouge layer sandwiched between two blocks; the block material is represented by a group of contact-bonded particles and the gouge is composed of unbonded particles (Fig. 3). Note that we invoke the one-way coupled assumption here (see Discussion section). (A similar scenario is also considered where the fault normal is aligned with the principal stress axis of $\sigma_{xx}$ and where a periodic boundary condition is used in the $z$ direction; see Supplementary Material [55].) For the gouge particles, the contact behavior between particles follows an

elastic–frictional contact law [42]. For the blocks, contact bonds are assigned to the particles. Once the tensile and shear strengths of a bond are exceeded, the bond breaks and the contact between the originally bonded pair of particles is described by the elastic–frictional contact law. To generate the block–gouge assembly, we first generate an isotropic initial packing under static equilibrium, following a widely adopted procedure [43]. Contact bonds are then included and boundary walls are used to apply an initial stress to the pack.

### E. Boundary conditions and system parameters

The boundary conditions are shown in Fig. 3. To initiate macroscopic fault slip, we apply load in the horizontal ($x$) direction using the left and right rigid walls with a constant strain rate ($\dot{\varepsilon}_h = \frac{\Delta x}{L_x \Delta t} = 7.8 \times 10^{-3}$ s$^{-1}$). We keep track of the horizontal stress $\sigma_h$ at the left and right wall boundaries. A zero displacement boundary is imposed for faces in the out-of-plane ($y$) direction ($u_y = 0$). On the top and bottom faces of the blocks, we use a servo-controlled vertical stress $\sigma_v$ of $1.0 \times 10^7$ Pa. We are interested in reproducing relative slip between the two blocks that minimizes finite-size effects, that is, slip along a plane that is parallel to the fault. To this end, we impose zero-displacement boundary conditions in the vertical ($z$) direction at the gouge layer ($u_z^g = 0$). To investigate the effect of pore pressure, we consider five different cases of pore-pressure distribution (Fig. 3). We slowly increase the pore pressure from zero to a predetermined final pressure ($p_t = 2.5 \times 10^7$ Pa for Case 1 and $0.5p_t = 1.25 \times 10^7$ for Case 4). Cases 2 and 3 are designed such that at all times, they have the same maximum pore pressure in the gouge as in Case 1 and have the same average pore pressure as in Case 4.

Case 1 The pore pressure increases uniformly (from 0 at zero horizontal strain) on both sides of the gouge layer to the final value ($p^L = p^R = p_t$) at horizontal strain of $3.1 \times 10^{-3}$, where $p^L$ and $p^R$ are the pore pressures on the left and right blocks, respectively.

Case 2 The pore pressure increases (from 0 at zero horizontal strain) on the left side of the gouge layer until $p^L = p_t$ at horizontal strain of $3.1 \times 10^{-3}$, while the pressure on the right side is held constant at zero value, $p^R = 0$. A linear gradient across the fault is maintained.

Case 3 Reverse of Case 2, with $p^L = 0$ and $p^R$ increases to $p_t$.

Case 4 Homogeneous pressure evolution, but only up to half the value of Case 1, $p^L = p^R = 0.5p_t$.

Case 5 Homogeneous pressure corresponding to the dry system with zero pore pressure, $p^L = p^R = 0$.

The simulation parameters are listed in Table I.

Even though our grain-scale coupled model captures the two-way coupling between flow and mechanical deformation, it is beneficial, from a standpoint of computational efficiency, to consider the assumption of one-way fluid to solid coupling in a given situation. Two-way coupling requires that pore geometry and throat conductance are updated at each time step, which is computationally intensive. Comparison of simulation results between the one-way and two-way coupling models justifies the simplifying assumption of one-way coupling (see discussions in Sec. IV). Thus, in the rest of our simulations we invoke this simplifying assumption and prescribe the pore pressure without solving for its evolution.

## III. RESULTS

In this section, we present numerical results for the five cases of pore pressure distribution. Our model setup resembles a triaxial configuration of a gouge layer friction experiment with pore pressure control. The gouge layer failure is driven by mechanical loading on the blocks. In the model, the grain rearrangement by rotation and intergranular slip is responsible for deformation of the gouge layer. Our focus is on the onset of shear failure under different pressure controls with special attention to cases where a discontinuity in pressure across the gouge layer exists, $p^L \neq p^R$. The fault normal stress $\sigma_n$ is calculated as $\sigma_n = \frac{1}{2}(\sigma_h + \sigma_v) + \frac{1}{2}(\sigma_h - \sigma_v)\cos 2\alpha$, where $\alpha$ is the angle of the gouge layer with respect to the horizontal and $\sigma_h$ and $\sigma_v$. For a more intuitive interpretation of the results, we follow the convention that compressive stresses are positive.

### A. Grain displacement and contact forces

Snapshots of grain displacement during the fault failure are presented in Fig. 4. These snapshots are taken at the same time point corresponding to a horizontal strain of $\varepsilon_h = 3.1 \times 10^{-3}$. It is evident from these snapshots that the spatial distribution of pore pressure strongly influences the deformation. For example, when the pore pressure is continuous across the fault (Case 1, Fig. 4(a)), the displacement pattern is largely symmetric, with the foot wall moving down, and the hanging wall moving up as a result of the imposed reverse faulting conditions. The slip of blocks initiates along the two gouge–block interfaces. At late times, strain localization is evident as the slip surfaces gradually shift towards the center of the gouge layer [56]. The faulting behavior is markedly different when the pressure is discontinuous across the fault(Cases 2–3, Fig. 4(c), (e)), accommodated with a strong pressure gradient within the gouge layer. For example, when $p^R > p^L$, the displacement of the hanging wall is significantly larger than that of the foot wall (Case 3, Fig. 4(e)). Moreover, slip is localized at the hanging-wall gouge–block interface, which is associated

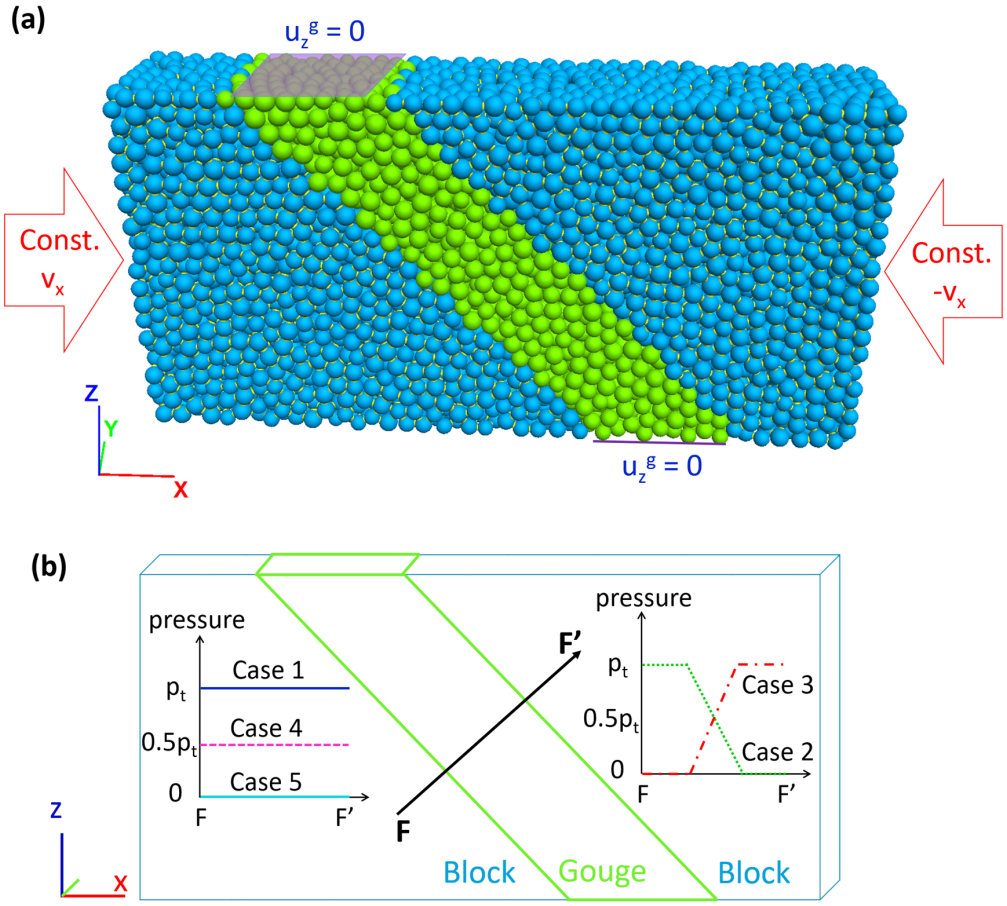


FIG. 3. (a), 3D block–gouge system composed of 7878 particles. The light green particles are unbonded, representing the gouge, while the blue particles are bonded, representing the blocks (fault walls). The origin of axes is placed at the center of the gouge layer. Rigid frictionless walls (not shown) are used to provide mechanical boundary conditions. Loading in the $x$ direction with constant velocity drives the system to slip failure. The front and back walls are assigned zero displacement condition ($u_y = 0$). To reproduce relative motion with respect to the gouge layer, we impose zero vertical displacement at the top and bottom of the gouge layer ($u_z^g = 0$). (b), Pore pressure cases. Cases 1, 4 and 5 represent continuous pressure across the fault, with Case 4 having a pressure half of that in Case 1, and Case 5 having zero pore pressure (dry system). Cases 2 and 3 represent discontinuous pressure across the fault, with a strong pressure gradient within the gouge layer.

TABLE I. Simulation parameters.

| **Parameters** | **Value** |
|---|---|
| Average grain diameter $\bar{d}$ | 0.002 m |
| min. and max. grain diameter $d_{\min}$, $d_{\max}$ | 0.0018, 0.0022 m |
| Grain-grain friction coefficient $\mu_{\text{g-g}}$ | 0.5 |
| Packing porosity $\phi$ | 0.35 |
| Contact normal stiffness $k_n^c$ | $5.0 \times 10^{10}$ N/m |
| Contact shear stiffness $k_s^c$ | $2.5 \times 10^{10}$ N/m |
| Contact bond tensile strength $T$, (mean $\pm$ std) | $(1.0 \pm 0.2) \times 10^9$ Pa |
| Contact bond shear strength $S$, (mean $\pm$ std) | $(1.0 \pm 0.2) \times 10^9$ Pa |
| Gouge layer width $w$ | 0.012 m |
| Gouge layer dip angle $\alpha$ | $45^\circ$ |
| Maximum pore pressure ($p_t$) | $2.5 \times 10^7$ Pa |
| Domain size $L_x$, $L_y$, $L_z$ | 0.08, 0.02, 0.05 m |

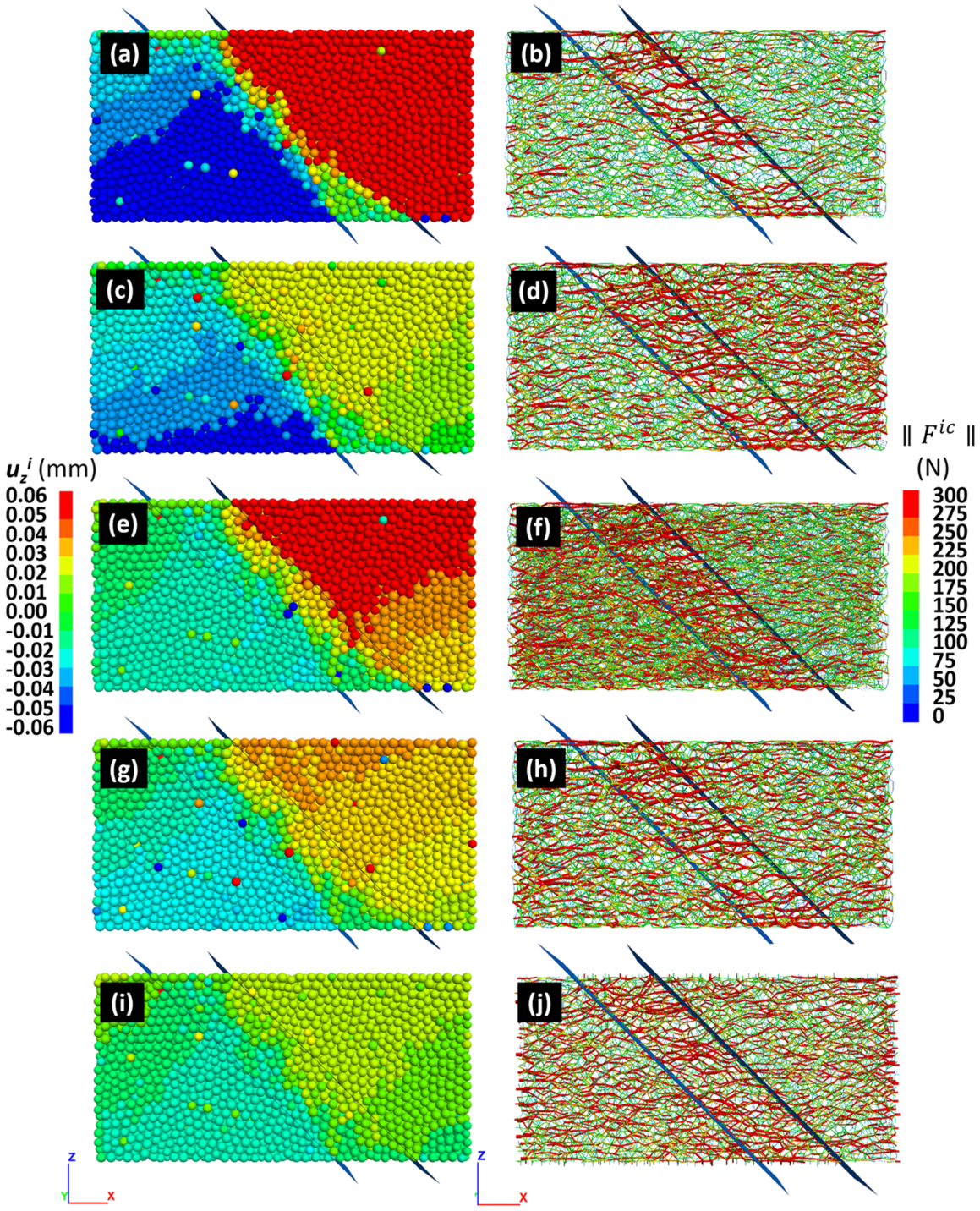


FIG. 4. Slip behavior for the block–gouge system. Particle displacement in the $z$ direction (left column) and contact force network with both color and link size representing force magnitude (right column) at horizontal strain $\varepsilon_h = 3.1 \times 10^{-3}$. (a)–(b): pore pressure Case 1; (c)–(d): Case 2; (e)–(f): Case 3; (g)–(h): Case 4; (i)–(j): Case 5.

with the higher pore pressure. In Case 4 where the pore pressure is half of that in Case 1, we observe a significant decrease of the magnitude of grain displacement in the $z$ direction. The simulation with dry condition (Case 5, Fig. 4(i)) produces the smallest relative vertical movement of the two blocks.

Contact force networks corresponding to the grain displacement snapshots discussed above are shown in the right column of Fig. 4. Pore fluid exerts pressure forces on the particles, which reduces the contact forces, with

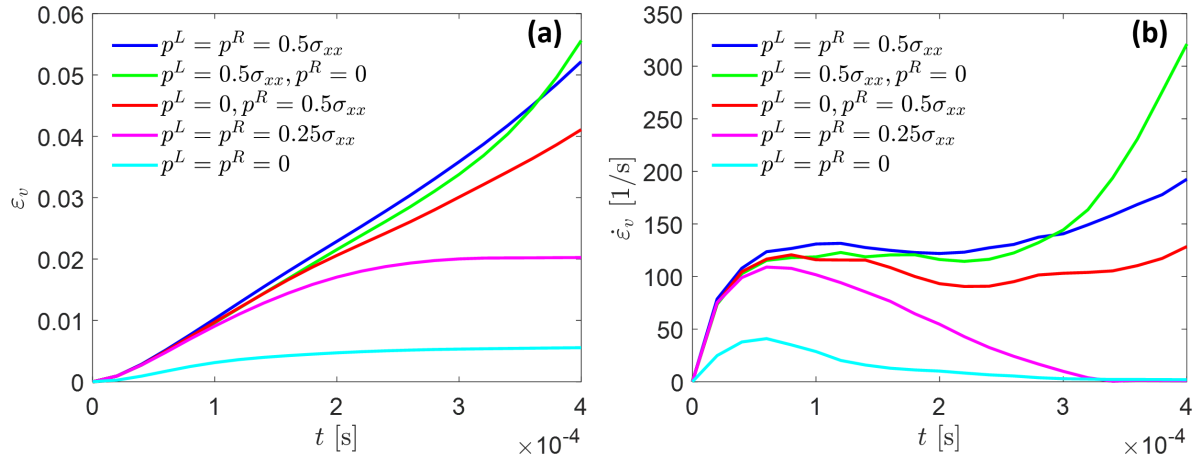


FIG. 5. Histogram of normal component of contact forces in the gouge layer for the scenario considered in the main text. (a) pore pressure case 1; (b) pore pressure case 3.

a macroscopic consequence of effective stress. The contact forces in the blocks are strongly influenced by the pore pressure distribution. When the pore pressure is uniform in the block–gouge–block system (Fig. 4(b), (h), (j)), the results show that the contact force network exhibits no overall difference between the left and right blocks. In contrast, for the inhomogeneous pore pressure cases (Fig. 4(d),(f)), the difference in the contact force network between the left and right blocks is apparent.

The horizontal loading initially compacts the gouge layer, which causes a rapid increase in the magnitude of contact forces [56]. The fabric of the contact force network evolves and chains of strong contact forces develop across the gouge layer as a result of loading. The contact force chains in the gouge layer are oriented roughly parallel to the loading direction and are distributed more or less evenly along the gouge layer (Fig. 4), indicating that the results are not strongly affected by finite-size effects. The number of contacts in the gouge layer drops by about 20%, and the maximum contact force magnitude increases by about an order of magnitude with only small differences between pore pressure cases (Fig. 5).

### B. Evaluation of equivalent fault pressure $p^f$

The transition from gouge layer compaction to slip is characterized by a sharp increase in vertical strain rate $\dot{\varepsilon}_v$ in all pore pressure cases (Fig. 6(a)). Here, $\dot{\varepsilon}_v$ is defined as the difference in vertical velocity between the top of the hanging wall block and the bottom of the footwall block, divided by $L_z$. Before slipping, the horizontal stress builds up rapidly, and the blocks dilate vertically, which characterizes the initial vertical strain rate as the gouge layer compacts. Comparison of cases 1, 4, and 5 (Fig. 6(a)) reveals that, when the pore pressure is lower, the onset of slip occurs at a later time and, hence, at a larger normal stress due to larger loading strain accumulated. In our scenario, the delayed onset of slip causes additional compaction of the gouge layer (as a result of horizontal loading), which strengthens the material.

One of our main interests is to see how the fault pressure should be evaluated in the block–gouge–block system with a pore pressure contrast between the two blocks. From Fig. 4 we observe that when there is a pore pressure difference across the fault, the onset of slip appears to be controlled by the *maximum* of pore pressure on either side of the gouge layer, $\max(p^L, p^R)$. Indeed, Fig. 6 also shows that the strain rate–stress curves for Cases 1, 2 and 3 turn sharply around the same normal stress and effective normal stress values, while Case 4 exhibits a much delayed turning point. Note that $\max(p^L, p^R)$ is identical for Cases 1, 2 and 3, while $(p^L + p^R)/2$ is the same for Cases 2, 3 and 4. Our result suggests that the onset of failure for Cases 2 and 3 behaves similarly to that for Case 1 rather than Case 4. This result indicates that in the effective stress principle $\sigma_n^{\text{eff}} = \sigma_n - p^f$, the fault pressure $p^f$ should be evaluated using the maximum of pore pressure on both sides instead of using the average.

In an additional scenario [55] where the fault normal is aligned with the direction of the principal stress $\sigma_{xx}$, the results confirm that the slip favors the side of the fault with a higher pore pressure when there is a substantial difference in pore pressure (Cases 2–3) between the two sides [55]. More importantly, by evaluating whether the system fails by slip or not, we can clearly distinguish Cases 2–3 from Case 4. Note that the arithmetic average of pore pressure in the fault gouge layer in Cases 2–3 equals to that in Case 4. This result further demonstrates the point that by assigning the arithmetic average of pressure to the situation where there is a strong pressure change across the fault one can make incorrect predictions of fault stability.

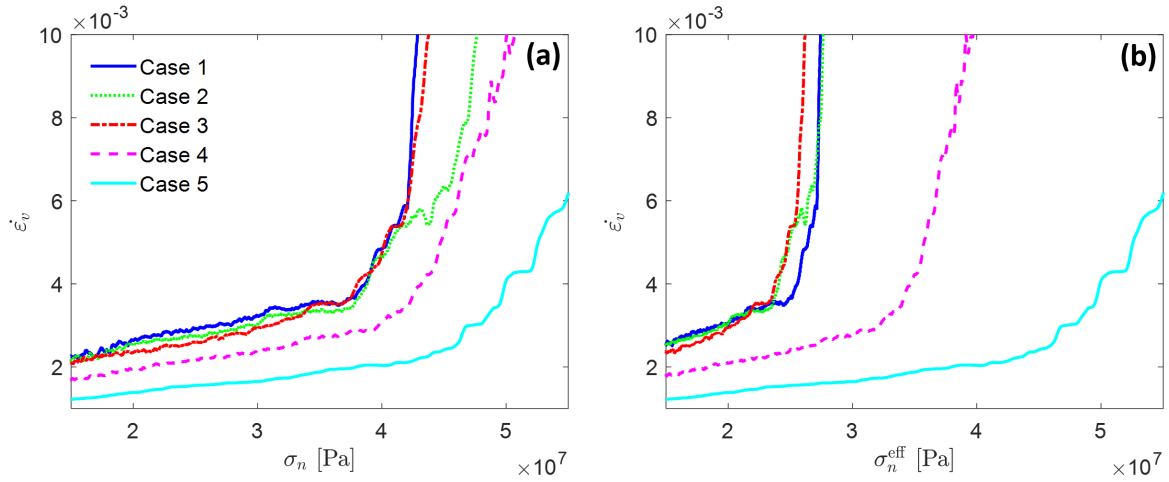


FIG. 6. (a) Vertical strain rate [$s^{-1}$] as a function of normal stress in the fault gouge. (b) Vertical strain rate [$s^{-1}$] as a function of *effective* normal stress $\sigma_n^{\text{eff}} = \sigma_n - p^f$ with fault pressure $p^f = \max(p^L, p^R)$.

## IV. DISCUSSION

In the simulations shown above, for computational efficiency we have made the simplification of assuming one-way fluid to solid coupling. The one-way coupling scheme here implies that the influence of solid matrix deformation on pore pressure is neglected, i.e., the first term on the left hand side of Eq. (7) is dropped. To test the validity of the assumption in our case of slip along a block–gouge interface, we have simulated fault slip using both the one-way and the two-way coupling methods (see Fig. 7). In both cases, a homogeneous initial pore pressure $p_0 = 0$ is assigned in the pack. The pore pressure evolution is traced in the two-way coupling case. The results show that the difference in grain displacement between the two simulations are indeed negligible (Fig. 7(b)–(c)). The slip between the block and the gouge reduces pore pressure along the shearing zone due to dilation (Fig. 7(d)), but the maximum pressure change due to mechanical shear (induced by loading on top of the block) is less than 1 kPa, almost four orders of magnitude smaller than the horizontal stress component.

To further substantiate that a one-way coupled approach is a good approximation in our problem setup, we compare two time scales in the system, the fluid pressure relaxation time scale $t_p$, and the pore deformation time scale $t_d$. The time scale $t_p$ can be calculated as $(L_x/2)^2/D_h$, where $L_x$ is the domain size in the horizontal direction and $D_h$ is the hydraulic diffusivity $k_0/(\beta_w \eta)$ with $k_0$ being the mean permeability (which can be estimated by running a Darcy flow simulation with prescribed pressure gradient), and $\beta_w$ and $\eta$ the compressibility and viscosity of water, respectively. The time scale $t_d$ is approximated as $d_p/v$, where $d_p$ is a representative pore diameter (which is taken as $0.1d$) and $v$ is a loading velocity. Substituting parameter values considered in this study, $L_x/2 = 2.0 \times 10^{-2}$ m, $k_0 = 1.0 \times 10^{-9}$ $m^2$, $\beta_w = 4.5 \times 10^{-10}$ $Pa^{-1}$, $\eta = 1.0 \times 10^{-3}$ Pa · s, and $v = 1.0 \times 10^{-2}$ m/s, we obtain $t_p$ on the order of $10^{-8}$s, and $t_d$ on the order of $10^{-2}$s. The separation of time scales in this system means that pore pressure will not change significantly due to fast dissipation through the pore space. This calculation justifies the one-way coupling assumption.

It should be pointed out that grain fragmentation, which can occur in a physical experiment involving pulverization, is not taken into account due to computational constraints. Grain size reduction during shear of fault gouge has been numerically studied using DEM under dry conditions, i.e., when the hydraulic coupling is not considered [32, 57]. The effect of fluid pressure on evolution of shearing fault gouge remains to be investigated in future studies.

## V. CONCLUSIONS

In summary, we have developed a 3D micromechanical model that couples a pore network flow (PNF) model to a discrete element model (DEM). The model couples fluid flow on the network of pores with mechanical deformation of the skeleton of solid grains. Pore fluid exerts pressure force onto the grains, the motion of which is solved using DEM. We have investigated the role of pore fluid pressure on slip failure of a block–gouge system. The fault zone is conceptualized as a gouge layer sandwiched between two blocks. Motivated by the problem of representing the fault pressure in the case of low across-fault permeability, we have studied the fault stability in the presence of a pressure discontinuity across the gouge layer, and compared it with the case of continuous (homogeneous) pore pressure.

Our micromechanical modeling results demonstrate the role of pore pressure in reducing the effective normal

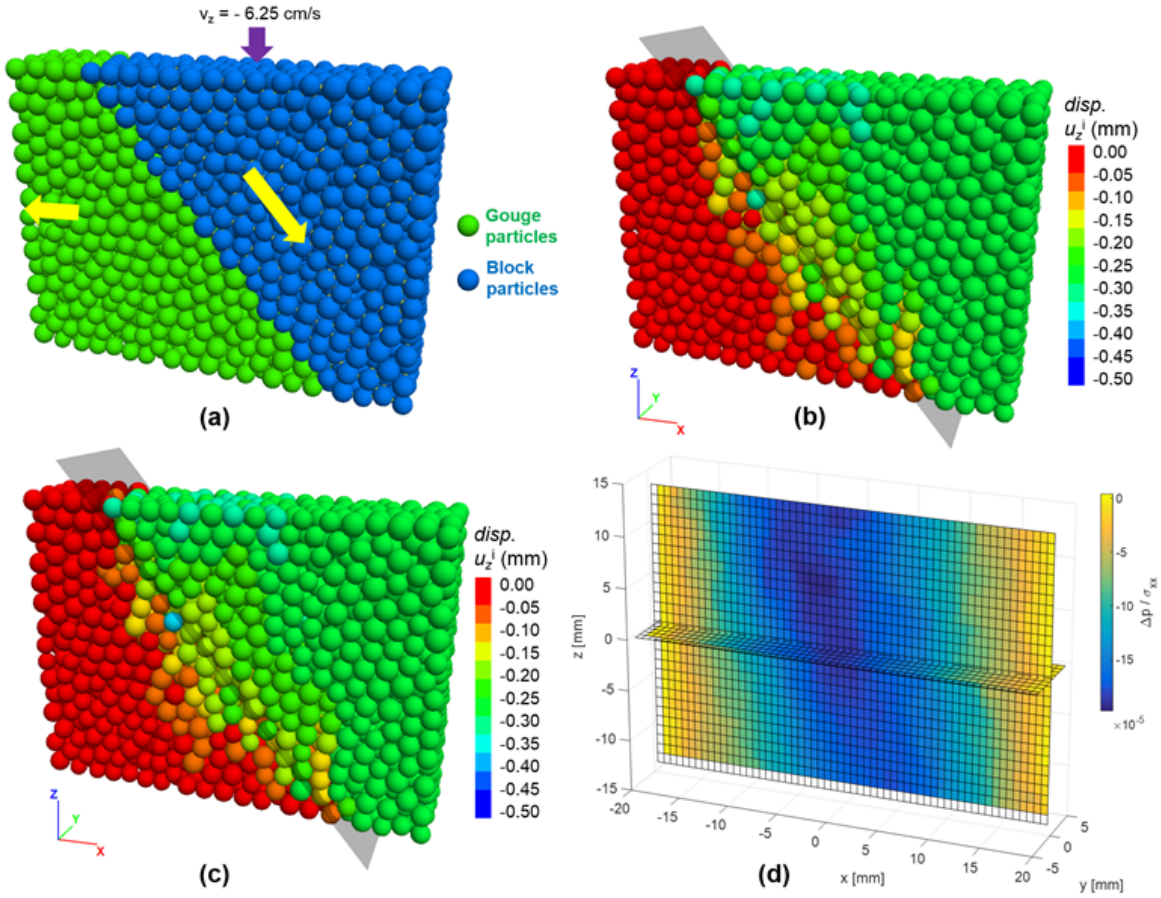


FIG. 7. Comparison of slip along a block–gouge interface between the fully coupled model and the simplified one-way coupled model. (a) The slip is simulated by providing a constant velocity to the block (as shown in blue); The left side and the right side of the system are given servo-controlled stress boundary The top and bottom boundaries of the gouge are given zero displacement condition; (b) Grain displacement ($z$ component) at t = 4ms simulated by the simplified model with one-way coupling; (c) Grain displacement ($z$ component) at t = 4ms simulated by the fully coupled model. (d) Pore pressure change (normalized by the horizontal stress) due to slip simulated by the fully coupled model; two cross sections ($y = 0$ and $z = 0$) are shown.

stress and causing earlier slip failure driven by mechanical loading. They show that, for the case of a pressure discontinuity across the fault, the onset of slip occurs earlier for the side with higher pore pressure, and that this onset appears to be controlled by the maximum pressure of both sides of the fault. Therefore, our results indicate that the fault pressure should be taken as the maximum pressure within the fault zone in a macroscopic hydromechanical coupling analysis where the effective stress on the fault is evaluated.

Natural fault zones are usually more complex than the simple system considered here. In a mature fault zone, multiple strands of fault gouge cores can develop (see [58] and references therein), indicating there may be multiple surfaces along which slip failure can occur. Multiple gouge cores also present a significant barrier for fluid flow across the fault zone. Our modeling results suggest that such a fault zone would fail first on the surface where the pore pressure is highest if the friction properties for the slip surfaces are similar. The results shed new light on the use of the effective stress principle and the Coulomb failure criterion in fault stability evaluation, and thus have important implications for seismic hazard assessment of subsurface fluid injection sites.

## ACKNOWLEDGMENTS

Z.Y. gratefully acknowledges financial support by the Swedish Research Council (VR) International Postdoc Program (Grant No. 637-2014-445). R.J. gratefully acknowledges financial support by the US Department of Energy (Award DE-SC0009286 and Award DE-FE0009738).

[1] J. H. Healy, W. W. Rubey, D. T. Griggs, and C. B. Raleigh, "The Denver earthquakes," Science **161**, 1301–1310 (1968).

[2] P. Segall, "Earthquakes triggered by fluid extraction," Geology **17**, 942–946 (1989).

[3] W. L. Ellsworth, "Injection-induced earthquakes," Science **341**, 1225942 (2013).

[4] Y. Guglielmi, F. Cappa, J.-P. Avouac, P. Herry, and D. Elsworth, "Seismicity triggered by fluid injection-induced aseismic slip," Science **348**, 1224–1226 (2015).

[5] C. W. Johnson, Y. Fu, and R. Bürgmann, "Seasonal water storage, stress modulation, and california seismicity," Science **356**, 1161–1164 (2017).

[6] C. A. J. Wibberley and T. Shimamoto, "Earthquake slip weakening and asperities explained by thermal pressurization," Nature **436**, 689–692 (2005).

[7] J. R. Rice, "Heating and weakening of faults during earthquake slip," Journal of Geophysical Research: Solid Earth **111**, B05311 (2006).

[8] R. C. Viesca and D. I. Garagash, "Ubiquitous weakening of faults due to thermal pressurization," Nature Geoscience **8**, 875–879 (2015).

[9] M. E. French, W. Zhu, and J. Banker, "Fault slip controlled by stress path and fluid pressurization rate," Geophysical Research Letters **43**, 4330–4339 (2016).

[10] M. Sawai, A. R. Niemeijer, O. Plümper, T. Hirose, and C. J. Spiers, "Nucleation of frictional instability caused by fluid pressurization in subducted blueschist," Geophysical Research Letters **43**, 2543–2551 (2016), 2015GL067569.

[11] W. Kurz, J. Imber, C. A. J. Wibberley, R. E. Holdsworth, and C. Collettini, "The internal structure of fault zones: fluid flow and mechanical properties," Geological Society, London, Special Publications **299**, 1–3 (2008).

[12] D. R. Faulkner and E. H. Rutter, "Can the maintenance of overpressured fluids in large strike-slip fault zones explain their apparent weakness?" Geology **29**, 503–506 (2001).

[13] H. Fossen, *Structural Geology*, 1st ed. (Cambridge University Press, Cambridge, 2010).

[14] C. H. Scholz, *The Mechanics of Earthquakes and Faulting*, 2nd ed. (Cambridge University Press, Cambridge, 2002).

[15] NRC, *Induced Seismicity Potential in Energy Technologies* (National Academies Press, Washington, D.C., 2013).

[16] F. Cappa and J. Rutqvist, "Impact of $CO_2$ geological sequestration on the nucleation of earthquakes," Geophysical Research Letters **38**, L17313 (2011).

[17] B. Jha and R. Juanes, "Coupled multiphase flow and poromechanics: A computational model of pore pressure effects on fault slip and earthquake triggering," Water Resources Research **50**, 3776–3808 (2014).

[18] R. Juanes, B. Jha, B. H. Hager, J. H. Shaw, A. Plesch, L. Astiz, J. H. Dieterich, and C. Frohlich, "Were the May 2012 Emilia-Romagna earthquakes induced? a coupled flow-geomechanics modeling assessment," Geophysical Research Letters **43**, 6891–6897 (2016).

[19] Z. Fan, P. Eichhubl, and J. F. W. Gale, "Geomechanical analysis of fluid injection and seismic fault slip for the mw4.8 timpson, texas, earthquake sequence," Journal of Geophysical Research: Solid Earth **121**, 2798–2812 (2016).

[20] J. W. Rudnicki and J. R. Rice, "Effective normal stress alteration due to pore pressure changes induced by dynamic slip propagation on a plane between dissimilar materials," Journal of Geophysical Research: Solid Earth **111**, 1–18 (2006).

[21] E. M. Dunham and J. R. Rice, "Earthquake slip between dissimilar poroelastic materials," Journal of Geophysical Research: Solid Earth **113**, 1–20 (2008).

[22] A. Tordesillas, "Force chain buckling, unjamming transitions and shear banding in dense granular assemblies," Philosophical Magazine **87**, 4987–5016 (2007).

[23] J. P. Bardet and J. Proubet, "A numerical investigation of the structure of persistent shear bands in granular media," Géotechnique **41**, 599–613 (1991).

[24] H. J. Tillemans and H. J. Herrmann, "Simulating deformations of granular solids under shear," Physica A: Statistical Mechanics and its Applications **217**, 261–288 (1995).

[25] E. Aharonov and D. Sparks, "Rigidity phase transition in granular packings," Physical Review E **60**, 6890–6896 (1999).

[26] M. Griffa, B. Ferdowsi, E.G. Daub, R.A. Guyer, P.A. Johnson, C. Marone, and J. Carmeliet, "Mesomechanical analysis of deformation characteristics for dynamically triggered slip in a granular medium," Philosophical Magazine **92**, 3520–3539 (2012).

[27] B. Ferdowsi, M. Griffa, R. A. Guyer, P. A. Johnson, C. Marone, and J. Carmeliet, "Microslips as precursors of large slip events in the stick-slip dynamics of sheared granular layers: A discrete element model analysis," Geophysical Research Letters **40**, 4194–4198 (2013).

[28] F. Kun, I. Varga, S. Lennartz-Sassinek, and I. G. Main, "Rupture cascades in a discrete element model of a porous sedimentary rock," Physical Review Letters **112**, 1–5 (2014).

[29] B. Ferdowsi, M. Griffa, R. A. Guyer, P. A. Johnson, C. Marone, and J. Carmeliet, "Acoustically induced slip in sheared granular layers: Application to dynamic earthquake triggering," Geophysical Research Letters **42**, 9750–9757 (2015).

[30] G. Pál, Z. Jánosi, F. Kun, and I. G. Main, "Fragmentation and shear band formation by slow compression of brittle porous media," Physical Review E **94**, 1–8 (2016).

[31] J. K. Morgan and M. S. Boettcher, "Numerical simulations of granular shear zones using the distinct element method: 1. shear zone kinematics and the micromechanics of localization," Journal of Geophysical Research **104**, 2703–2719 (1999).

[32] Z. Zhao, "Gouge particle evolution in a rock fracture undergoing shear: a microscopic DEM study," Rock Mechanics and Rock Engineering **46**, 1461–1479 (2013).

[33] D. F. Boutt, B. K. Cook, B. J. McPherson, and J. R. Williams, "Direct simulation of fluid-solid mechanics in porous media using the discrete element and lattice-Boltzmann methods," Journal of Geophysical Research: Solid Earth **112**, B10209 (2007).

[34] A. Komoróczi, S. Abe, and J. L. Urai, "Meshless numerical modeling of brittle–viscous deformation: first results on boudinage and hydrofracturing using a coupling of

discrete element method (DEM) and smoothed particle hydrodynamics (SPH)," Computational Geosciences **17**, 373–390 (2013).

[35] M. Mansouri, M. S. El Youssoufi, and F. Nicot, "Numerical simulation of the quicksand phenomenon by a 3d coupled discrete element-lattice boltzmann hydromechanical model," International Journal for Numerical and Analytical Methods in Geomechanics **41**, 338–358 (2017).

[36] K. D. Kafui, C. Thornton, and M. J. Adams, "Discrete particle-continuum fluid modelling of gas–solid fluidised beds," Chemical Engineering Science **57**, 2395–2410 (2002).

[37] L. Li and R. M. Holt, "Particle scale reservoir mechanics," Oil and Gas Science and Technology **57**, 525–538 (2002).

[38] A. K. Jain and R. Juanes, "Preferential mode of gas invasion in sediments: Grain-scale mechanistic model of coupled multiphase fluid flow and sediment mechanics," Journal of Geophysical Research: Solid Earth **114**, B08101 (2009).

[39] E. Catalano, B. Chareyre, and E. Barthélémy, "Pore-scale modeling of fluid-particles interaction and emerging poromechanical effects," International Journal for Numerical and Analytical Methods in Geomechanics **38**, 51–71 (2014).

[40] ITASCA, *PFC3D, v4.1: Theory and Background*, Itasca Consulting Group, Inc., Minneapolis, MN (2015).

[41] T. W. Patzek and D. B. Silin, "Shape factor and hydraulic conductance in noncircular capillaries: I. One-phase creeping flow," Journal of Colloid and Interface Science **296**, 295–304 (2001).

[42] P. A. Cundall and O. D. L. Strack, "A discrete numerical model for granular assemblies," Géotechnique **29**, 47–65 (1979).

[43] D. O. Potyondy and P. A. Cundall, "A bonded-particle model for rock," International Journal of Rock Mechanics and Mining Sciences **41**, 1329–1364 (2004).

[44] C. Marone, "Laboratory-derived friction laws and their application to seismic faulting," Annual Review of Earth and Planetary Sciences **26**, 643–696 (1998).

[45] G. Chambon, J. Schmittbuhl, and A. Corfdir, "Frictional response of a thick gouge sample: 1. Mechanical measurements and microstructures," Journal of Geophysical Research: Solid Earth **111**, B09308 (2006).

[46] B. A. Verberne, C. He, and C. J. Spiers, "Frictional properties of sedimentary rocks and natural fault gouge from the Longmen Shan fault zone, Sichuan, China," Bulletin of the Seismological Society of America **100**, 2767–2790 (2010).

[47] A. H. Kohli and M. D. Zoback, "Frictional properties of shale reservoir rocks," Journal of Geophysical Research: Solid Earth **118**, 5109–5125 (2013).

[48] M. M. Scuderi, B. M. Carpenter, P. A. Johnson, and C. Marone, "Poromechanics of stick-slip frictional sliding and strength recovery on tectonic faults," Journal of Geophysical Research: Solid Earth **120**, 6895–6912 (2015).

[49] R. M. Kurzawski, M. Stipp, A. R. Niemeijer, C. J. Spiers, and J. H. Behrmann, "Earthquake nucleation in weak subducted carbonates," Nature Geoscience **9**, 717–722 (2016).

[50] J. H. Dieterich, "Modeling of rock friction: 1. Experimental results and constitutive equations," Journal of Geophysical Research: Solid Earth **84**, 2161–2168 (1979).

[51] A. Ruina, "Slip instability and state variable friction laws," Journal of Geophysical Research: Solid Earth **88**, 10359–10370 (1983).

[52] D. A. Geller, R. E. Ecke, K. A. Dahmen, and S. Backhaus, "Stick-slip behavior in a continuum-granular experiment," Physical Review E **92**, 060201 (2015).

[53] N. Brodu, J. A. Dijksman, and R. P. Behringer, "Spanning the scales of granular materials through microscopic force imaging," Nature Communications **6**, 6361 (2015).

[54] R. C. Hurley, S. A. Hall, J. E. Andrade, and J. Wright, "Quantifying interparticle forces and heterogeneity in 3D granular materials," Physical Review Letters **117**, 098005 (2016).

[55] "See supplemental material at [url will be inserted by publisher] for simulation results for the scenario of fault orientation aligned with the principal stress directions (Part III),".

[56] "See supplemental material at [url will be inserted by publisher] for movies of grain displacement and contact forces (Part II),".

[57] K. Mair and S. Abe, "3D numerical simulations of fault gouge evolution during shear: Grain size reduction and strain localization," Earth and Planetary Science Letters **274**, 72 – 81 (2008).

[58] D. R. Faulkner, C. A L Jackson, R. J. Lunn, R. W. Schlische, Z. K. Shipton, C. A J Wibberley, and M. O. Withjack, "A review of recent developments concerning the structure, mechanics and fluid flow properties of fault zones," Journal of Structural Geology **32**, 1557–1575 (2010).